Published in final edited form as:

IEEE Trans Ultrason Ferroelectr Freq Control. 2012 April ; 59(4): 648–659. doi:10.1109/TUFFC.2012.2243.

Harmonic Spatial Coherence Imaging: An Ultrasonic Imaging Method Based on Backscatter Coherence

Jeremy J Dahl, Member, IEEE, **Marko Jakovljevic**, **Gianmarco F. Pinton**, and **Gregg E. Trahey, Member, IEEE**

J. J. Dahl, M. Jakovljevic, and G. E. Trahey are currently with the Department of Biomedical Engineering, Duke University, Durham, NC. G. E. Trahey and is also with the Department of Radiology, Duke University Medical Center, Durham, NC. G. F. Pinton is with the Institut Langevin at ESPCI, Paris, France.

Jeremy J Dahl: jeremy.dahl@duke.edu

Abstract

HSCI and SLSC imaging less sensitive to clutter because it has low spatial coherence. The method is based on the coherence of the second harmonic backscatter. Because the same signals that are used to construct harmonic B-mode images are also used to construct HSCI images, the benefits obtained with harmonic imaging are also applicable to HSCI. Harmonic imaging has been the primary tool for suppressing clutter in diagnostic ultrasound imaging, however second harmonic echoes are not necessarily immune to the effects of clutter. HSCI and SLSC imaging are less sensitive to clutter because it has low spatial coherence. Harmonic Spatial Coherence Imaging shows favorable imaging characteristics such as improved contrast-to-noise ratio (CNR), improved speckle signal-to-noise ratio (SNR), and better delineation of borders and other structures compared to fundamental and harmonic B-mode imaging. CNRs of up to 1.9 were obtained from *in vivo* imaging of human cardiac tissue with HSCI, compared to 0.6, 0.9, and 1.5 in fundamental B-mode, harmonic B-mode, and SLSC imaging, respectively. *In vivo* experiments in human liver tissue demonstrated SNRs of up to 3.4 for HSCI compared to 1.9 for harmonic B-mode. Nonlinear simulations of a heart chamber model were consistent with the *in vivo* experiments.

I. Introduction

In conventional ultrasound imaging, delay-and-sum beamformers are used to image the magnitude of backscattered echoes. Many publications have described the resolution, signal-to-noise ratio, speckle, and other characteristics associated with this type of imaging system [1, 2]. We have recently introduced a new imaging method, called Short-Lag Spatial Coherence (SLSC) imaging, that provides images that look similar to conventional B-mode imaging but use lateral spatial coherence as the basis of image formation rather than echo brightness [3, 4]. This method yields similar resolution to B-mode imaging, however the physical basis for contrast, resolution, and image texture are different [3, 4]. Given the significant number of poor quality ultrasound exams and their increasing number due to body habitus over the last two decades [5–8], there is a need for better ultrasonic imaging methods.

Harmonic imaging is one such method that was introduced within the last 15 years as a method to improve upon existing ultrasonic imaging methods [9–11]. It is based on the nonlinear propagation of pressure waves, which generates frequency components at integer multiples of the transmitted frequency. Harmonic imaging has become a mainstay in ultrasound, where harmonic imaging is often the default mode for patients and conventional imaging is utilized only when harmonic imaging does not provide sufficient image quality or imaging depth. A wide range of studies have demonstrated its improvements in image quality over conventional B-mode imaging [12–14].

Imaging methods based on the quantification of the coherence of backscatter have also been proposed to improve upon existing ultrasonic imaging methods. Mallart and Fink [15] introduced a parameter, C (this parameter was later redefined as the ’coherence factor’ by Hollman et al. [16]), that described the focusing characteristics of an imaging system. The coherence factor is a ratio of the coherent intensity to the total incoherent intensity and its particular application was to provide a measure, in a general sense, of the alignment of echoes after they are time-delayed according to time-of-flight differences. The coherence factor peaks at 2/3 for perfect focusing of a large speckle-generating target and decreases with increasing aberration. Liu and Waag [17] introduced a similar metric, called the waveform similarity factor (WSF), which was used to estimate the optimal position of a phase screen for aberration correction. Li and Li [18] introduced a modified version of Mallart and Fink’s coherence factor, called the generalized coherence factor (GCF), that applies a k-space filter to the echo signals to remove off-axis scatterer influence on the coherence factor measurement. The GCF was then used to weight the B-mode image to reduce clutter from phase aberrations. This method is similar to the aberration correction technique PARCA [19] in that it attempts to suppress the high sidelobes of the ultrasonic beam induced by aberration. The phase coherence factor (PCF) and sign coherence factor (SCF) introduced by Camacho et al. [20] are similar to these sidelobe suppression techniques, however the PCF and SCF are based on the standard deviation of the phase of the echo across the aperture rather than a ratio of coherence to incoherence.

We present an adaptation of the SLSC imaging technique to harmonic imaging. This technique is unique compared to previous coherence-based image metrics and techniques in that the resulting images are derived directly from the spatial coherence function of the echoes themselves, rather than a weighted or otherwise modified B-mode image. We demonstrate, using a full-wave simulation program and *in vivo* examples, that the method yields superior imaging metrics compared to conventional delay-and-sum imaging and is robust in the presence of clutter.

Clutter is often observed in poor quality ultrasound images as an overlying haze or fill-in that obscures organs, lesions, and blood vessels, and leads to inadequate visualization of anatomy or function. Clutter is often attributed to reverberation among tissue layers, scattering from off-axis targets or side and grating lobes, and aberrations. Reverberation clutter occurs when an acoustic wave reflects multiple times between layers of tissue, and creates a diffuse overlying haze over the image [21]. Aberrations are distortions of the acoustic wave, which can occur from local deviations in sound speed or attenuation. Aberrations resulting from changes in sound speed decrease resolution and contrast, and increase off-axis scattering. A recent study has demonstrated that both reverberation and phase aberration play significant roles in generating image clutter and degrading image quality [22].

Although methods of clutter reduction are commonly applied in Doppler imaging via the use of wall filtering, relatively few techniques exist for removing clutter from B-mode imaging [23, 24]. Both Lediju et al. [23] and Mauldin et al. [24] use filtering methods across image frames. These methods rely on the clutter being stationary relative to moving tissue, much like wall filtering relies on the clutter being stationary relative to moving blood signal in Doppler imaging. Lediju et al. use a compression technique, similar to that used in elastographic imaging methods, that relies on the assumption that clutter from near field tissue layers remains stationary compared to the tissue moving under compression. Mauldin et al. apply a principle component analysis technique to moving cardiac tissue with the same assumption as Lediju. While both methods work well, they reduce clutter only from reverberation within tissues close to the transducer and they rely on some form of motion of the tissue. Current clinical practices to reduce image clutter involve manual compression of the skin and fat layers with the transducer and the use of harmonic imaging. Pinton et al. [22] have shown that the major source in image quality improvement with harmonic imaging is the reduction in clutter originating from reverberation within proximal tissue layers.

Numerous studies have attempted to correct for aberrations and its resulting effects [17, 19, 25–28]. These methods are capable of improving contrast and resolution of targets and decrease clutter from off-axis scattering, but clinical studies of phase aberration correction typically demonstrate only moderate improvement in contrast and contrast-to-noise ratio (CNR) [28, 29]. Pinton et al. [22] demonstrated in simulation studies that to achieve large improvements *in vivo*, aberration correction must also be accompanied by clutter suppression, although aberration correction techniques are typically degraded by the effects of reverberation clutter and off-axis scattering [30].

II. Short-Lag Spatial Coherence (SLSC) Imaging

In conventional pulse-echo ultrasound, the echo scattered from a point in tissue spreads out spatially as it travels back to the transducer. Spatial coherence is a measure of how similar the echo is at any two points in space. It is a function of *lag*, which is the distance between two spatial points (e.g. $x_1 - x_2$), as opposed to a function of position. The lateral spatial coherence of backscattered ultrasound waves can be predicted by the van Cittert Zernike (VCZ) theorem. The VCZ theorem states that the spatial covariance (one measure of spatial coherence) of a wavefront produced by an incoherent source is the scaled Fourier transform of the source’s intensity distribution [31]. Because the original VCZ theorem was developed for optics, Mallart and Fink [32] demonstrated that the VCZ theorem could be applied to pulse-echo ultrasound and that diffuse scatterers will create an incoherent source. The intensity distribution is then the square of the product of the lateral transmit beam pressure and the lateral backscatter, or source, function. For homogeneous tissue that is made of diffuse scatterers, application of the VCZ theorem shows that the spatial coherence function decreases linearly from 1 at a lag of 0, to 0 at a lag of A, where A is the width of the transmit aperture. This theoretical model of spatial covariance has been previously validated with simulations and tissue-mimicking phantoms [32–34].

SLSC imaging differs substantially from existing coherence metrics (e.g GCF, PCF, etc.) in that images are formed from a direct measure of the spatial coherence function. This is accomplished by computing the normalized cross-correlation of the echoes that have been received by the transducer and time-delayed according to time-of-flight differences:

$$\widehat{R}(m)=\frac{1}{N-m}\sum_{i=1}^{N-m}\frac{\sum_{n=n_1}^{n_2} s_i(n)s_{i+m}(n)}{\sqrt{\sum_{n=n_1}^{n_2} s_i^2(n)\sum_{n=n_1}^{n_2} s_{i+m}^2(n)}} \qquad (1)$$

Here, $s_i(n)$ is the time-delayed signal received by the i^{th} element of a receive aperture with N elements and pitch d (see Fig. 1(b)). For simplicity, we make the receive aperture equal in size to the transmit aperture, such that $(N-1)d = A$. m is the lag normalized by d, n is the time sample, and $n_2 - n_1$ is on the order of a wavelength, in samples. When the lag is normalized by d, the lag is given in terms of number of elements, which simplifies computational effort. Intuitively, however, it is easier to think of the lag normalized by the transmit aperture width A, because the spatial coherence tends to zero beyond distances A for most imaging conditions. In this case, the spatial coherence is a function of lag ℓ, a fraction of the transmit aperture with maximum lag equal to 1 (see Fig. 1(f)).

A metric, called the short-lag spatial coherence (SLSC) value, V_{slsc}, is created as the integral of the spatial coherence function up to lag Q (Fig. 1(g)):

$$V_{slsc}=\int_{0}^{Q}\widehat{R}(\ell)d\ell \approx \sum_{m=1}^{M}\widehat{R}(m) \tag{2}$$

where Q is expressed as a fraction of the transmit aperture and is typically in the range of 0.05–0.3, which is defined as the short-lag region of the spatial coherence function. When implementing this calculation on echo data acquired by real transducers, the right hand side of Eq. 2 is preferred, where M is the fraction of the transmit aperture given as an integer number of element spacings. The denominator term in Eq. 1 is a normalization term that minimizes the impact of echo magnitude in SLSC image formation. Thus, the resulting images are dependent on the ratio of coherent or partially-coherent signal to the incoherent signal.

The process of forming an SLSC image is relatively simple and is diagrammed in Fig. 1 and compared to the process of forming B-mode images. An SLSC image is formed by computing the spatial coherence function (Eq. 1) and the SLSC integral (Eq. 2) at every depth sample for every pulse-echo across a field-of-view (FOV). The resulting V_{slsc} value for each point is then used as the pixel values in the image.

A. Harmonic Spatial Coherence Imaging (HSCI)

SLSC imaging can readily be applied to the second-harmonic echo signals. In this case, either second-harmonic filtering [10] or pulse inversion [35] is performed on the channel signals of the ultrasound system to obtain the second-harmonic signals (see Fig. 1(c)) to which Eqs. 1 and 2 can then be applied. Note that in conventional harmonic imaging, these operations are performed on the beamsummed RF signals rather than the individual channel signals. The application of the SLSC imaging technique to the harmonic signals will be referred to as Harmonic Spatial Coherence Imaging (HSCI) whereas application of the same technique to the fundamental signals will simply be referred to as SLSC imaging.

III. Methods

A. Simulated Heart Chamber

A full-wave, nonlinear acoustic (FWNA) wave propagation method [36] was used to generate simulated images of a heart chamber to demonstrate the Harmonic Spatial Coherence Imaging method. This simulation program is capable of creating realistic ultrasound images from complex models of human tissue and includes the major image degrading effects in ultrasound, such as reverberation clutter, off-axis scattering, and phase aberrations.

The heart chamber was modeled as a 40×20mm anechoic oval surrounded by diffuse scatterers with a density of 12 scatterers per resolution cell. Two thrombi, modeled as 5mm circular regions of diffuse scatterers, were placed within the chamber and given a −12 dB scattering strength relative to the surrounding wall scatterers. The thrombi were placed at depths of 35 and 45mm. A control simulation was performed, where scatterers were placed between the transducer and the heart chamber and the tissue was given the properties of “ideal” tissue (i.e. a speed of sound of 1540m/s, a density of 1 g/mL, an attenuation of 0.5

dB/cm·MHz, and a nonlinear parameter of 9). A second simulation was performed, where a model of human skin and fat layers based on histological samples [37, 38] was placed between the transducer and the heart chamber. This model includes the complex geometry of fat and connective tissue layers, which induce reverberation clutter and aberration in the simulation. Both simulations utilize a 128-element phased-array with a pitch of 0.308mm. An F/2 transmit was employed with this array at a frequency of 2.5MHz. The images are created using two transmit focal zones, at 4 and 6 cm, to maximize image quality over depth.

RF channel signals were generated by sampling the acoustic field of the FWNA wave simulator at the transducer surface. The channel signals were dynamically time-delayed according to time-of-flight differences. Bandpass filtering with a center frequency of 5MHz and a bandwidth of 60% was applied to the channel signals to obtain the second harmonic channel signals. The fundamental and harmonic channel signals were then used to form B-mode, SLSC, harmonic B-mode, and HSCI images. SLSC and HSCI images were implemented by applying Eqs. (1) and (2) at every depth sample for every image line. The value of Q used for the SLSC and HSCI images was 0.325. Custom depth-dependent gain was applied to the SLSC and HSCI images in order to normalize the image brightness with the depth-dependent gain was computed by applying

$$G(z)=C(z)(1-g(z)+\max[g(z)]) \qquad (3)$$

where $g(z)$ is the mean image brightness as a function of depth and $C(z)$ is a custom, depth-dependent multiplication factor in the range of 0.5–2, and used much like the sliders in a TGC control where the same level of gain is applied to a wide depth range.

B. In Vivo Human Abdominal and Cardiac Applications

A Siemens Acuson S2000™ ultrasound scanner (Siemens Medical Solutions USA, Inc., Issaquah, WA) and the Axius Direct™ Ultrasound Research Interface [39] was used to acquire the necessary channel signals for SLSC image formation. Channel signals were acquired from the liver and kidney of one subject with a 128-element, Siemens 4C1 transducer and from the heart of another subject with a 96-element, Siemens 4P1 transducer using a custom-programmed, synthetic receive aperture technique [40]. Briefly, the synthetic aperture method acquires the individual channel signals by transmitting a pulse from a specified transmit aperture and recording the RF echo on an individual element. The same transmit beam configuration (aperture, apodization, etc.) is utilized on subsequent transmits until the signals on all receive elements are acquired. The process is repeated for the next imaging location, until the channel signals for all transmit beams (and thus image lines) are acquired.

64 element signals were acquired for each of 54 image lines in the liver and kidney and 12 image lines were acquired in the heart, where the acquired channel signals were centered around the transmit aperture. The number of image lines is limited due to programming constraints with respect to the liver and kidney images, and highly dynamic motion of cardiac tissue with respect to the heart images. Pulse inversion was employed such that each element acquired a positive and negative version of the echo for formation of the second harmonic signal. Using a single focal depth, an F/2 transmit system was employed with a transmit frequency of 1.8MHz for the 4C1 abdominal array and an F/5 transmit at a frequency of 2MHz was utilized with the 4P1 cardiac array. The F/#s used here were increased compared to that used by Lediju et al. [3] (F/1.5) in order to extend the depth-of-field and improve the imaging capabilities of SLSC and HSCI imaging. The beamformed radio-frequency (RF) signals for the full B-mode image, with pulse-inversion, were acquired concurrently to compare with the SLSC and HSCI images. The channel signals were dynamically time-delayed according to expected time-of-flight differences and then

bandpass filtered about the center and second harmonic frequencies. SLSC and HSCI images were implemented using the same methods as the simulation data. In all *in vivo* images, the value of Q used was 0.093.

Contrast, contrast-to-noise ratio (CNR), and speckle signal-to-noise ratio (SNR) were measured from the thrombi in the simulated echoes and from blood vessels and background liver tissue in the *in vivo* images. Contrast, CNR, and speckle SNR were measured using $20\ \log(\langle S_i \rangle / \langle S_o \rangle), |(\langle S_i \rangle - \langle S_o \rangle| / \sqrt{\sigma_i^2 + \sigma_o^2}, and\ \langle S_o \rangle / \sigma_o$, respectively. S_i and S_o are the magnitudes inside and outside the target, respectively, σ_i and σ_o are the standard deviations of the pixel values in the target and background areas, and $\langle \cdot \rangle$ indicates a spatial mean of the pixel values. For contrast and CNR, the measures were taken from laterally adjacent regions so that depth-dependent effects did not bias the measurements. The speckle SNR measurements were taken from the same background region used for the contrast and CNR measurements.

IV. Results

Fundamental and harmonic B-mode and SLSC images of the simulated heart chamber and its two thrombi without intervening tissue layers are shown in Fig. 2 with contrast, CNR, and speckle SNR of the thrombus at 45mm shown in Tab. I. These images directly compare fundamental and harmonic imaging to SLSC and HSCI imaging under ideal imaging conditions. Both thrombi are easily visible in all images. The texture of the thrombi and background tissue in the SLSC and HSCI images are distinctly smoother than the B-mode images. Furthermore, the SLSC and HSCI images produce clearer delineation of the space and borders between the thrombi and the heart wall. The B-mode images are compressed using a logarithmic grayscale mapping and limited to show 60 dB of dynamic range. Unlike the B-mode images, the SLSC and HSCI images are not compressed and show nearly the full linear scale of the image (ranging from 0 to 95% of the maximum value). All following SLSC and HSCI images are shown in this manner. Depth-dependent gain is also applied to the SLSC and HSCI images in order to equalize the brightness in the image with depth.

Fig. 3 shows the same images as in Fig. 2 but with intervening skin, fat, and connective tissue between the transducer and the heart chamber. Neither thrombus is visible in the fundamental B-mode image, and extensive clutter obscures the proximal boundary of the chamber. In the SLSC image, the clutter in the chamber is significantly decreased, the contrast and CNR of the thrombus at 45mm is markedly improved, and the borders of the heart chamber are better delineated. Harmonic B-mode imaging (Fig. 3(c)) greatly reduces clutter resulting from the near-field tissue layers, so the thrombus at 45mm depth becomes significantly more visible compared to the fundamental B-mode and SLSC images. However, the visibility of the thrombus at 35mm remains poor, reverberation clutter still degrades the proximal boundary, and off-axis clutter is present on the lateral borders. The harmonic SLSC image shows the largest contrast and CNR of all images, and delineates borders better than the harmonic B-mode. In addition, the thrombus at 35mm becomes significantly more visible and very little clutter signal is present. The B-mode images are shown with 60 dB of dynamic range. The contrast, CNR and speckle SNR of the thrombus at 45mm is shown in Tab. I.

Fig. 4(a) displays a fundamental B-mode image of the liver of a 57-year-old male, created from the positive beamformed RF signals acquired from the 4C1 transducer focused at 10 cm. The image contains a significant amount of clutter that obscures many of the smaller features in the image. The large vessel in the distal part of the liver is easily apparent, and some vessels on the left side of the image are also well visualized. A vessel traversing the liver vertically from 10 to 13 cm is difficult to observe. The *in vivo* B-mode images depicted here and in the following images are displayed with bandpass filtering and logarithmic compression and limited in dynamic range such that the vessels show as much visual contrast as possible without degrading the remaining diagnostic information from the image. In Fig. 4(a), the B-mode image is shown with 35 dB of dynamic range. All images are cropped in order to display only the diagnostically useful information. We would note that the B-mode images shown here are generated from minimal processing of the raw beamformed RF signals while images typically shown “on-screen” include many proprietory post-processing filters or nonlinear effects that improve overall image quality over that seen here (although these filters and nonlinear effects may not reduce clutter).

In Fig. 4(b), the SLSC image is overlaid on the B-mode image in the center of the image, where the arrows demarcate the boundaries of the SLSC image. Because of the limitations imposed by creating custom beam sequences on commercial ultrasound scanners, only a small sector of the total FOV could be acquired for SLSC image formation. The SLSC image sector in Fig. 4(b) demonstrates a considerable reduction in clutter, particularly in the high-contrast vessels. The vertically aligned vessel at 10–13 cm depth is much more discernible, where the contrast improves from 3 dB in the B-mode image to 7 dB in the SLSC image.

Fig. 4(c) displays the harmonic B-mode image, created from the sum of the positive and negative pulses acquired from the custom, pulse-inversion, synthetic aperture sequence. The harmonic B-mode image shows better visualization of the vertically aligned vessel than the fundamental B-mode image, however considerable clutter still obscures this vessel. Application of the SLSC imaging technique to the second harmonic signals is shown in Fig. 4(d), where arrows demarcate the boundaries of the HSCI image. The contrast of the vertical vessel is 5 dB in the harmonic B-mode image compared to 8 dB in the HSCI image. The contrast-to-noise ratios (CNR) of this vessel and the speckle signal-to-noise ratio (SNR) of the liver tissue is shown in Tab. II. The CNR and SNR of the SLSC and HSCI images is significantly greater than their corresponding B-mode images.

Fig. 5 demonstrates the spatial coherence functions for two echoes originating from points in Fig. 4(a): one in the liver tissue and one from the lumen of the vessel at 11 cm. These spatial coherence functions are compared to that of an echo from diffuse scatterers in a calibrated tissue mimicking phantom (Model 054GS, Computerized Imaging Reference Systems, Norfolk, VA). The diffuse scatterers (dashed line) generate a spatial coherence function that is roughly a straight line decreasing from 1 to 0, which is the well-known result predicted by the VCZ theorem. The spatial coherence from liver tissue should ideally match that of the diffuse scatterers, however, a significant drop in coherence is observed at the lags near zero, followed by a nonlinear decrease in coherence for both the fundamental and harmonic echoes. Note that the spatial coherence of the second harmonic signal from the same echo shows greater coherence than the fundamental signal. An echo from the vessel lumen shows coherence that is 1 at zero-lag and immediately drops to zero thereafter.

Fig. 6 displays fundamental and harmonic B-mode and SLSC images of the right kidney in a 57-year-old male. The fundamental images are created from the positive pulses of the synthetic aperture sequence. In the fundamental B-mode image 45 dB of dynamic range is shown. The pelvic region of the kidney is apparent by the bright echoes in the middle of the kidney, but few other features are evident. The pelvic region of the kidney contains many structures such as the major and minor callyces and blood vessels. In the SLSC image, a significant reduction in clutter is obtained, more features of the pelvic region are visible, and the distal border of the kidney is more apparent. In the harmonic B-mode image, the clutter is somewhat reduced, but the details of the pelvic region are not significantly more apparent than the fundamental B-mode image. The HSCI image shows the best overall quality of the kidney and its pelvic region. Specifically, the HSCI image denotes a contrasting region in the proximal region of the kidney between 8 and 10 cm. This contrasting region is consistent with the medulla of the kidney, and often difficult structure to detect based on its low contrast with the kidney's cortex.

SLSC and HSCI imaging was applied to *in vivo* imaging of the human heart in Fig. 7. Fig. 7(a) shows a fundamental B-mode image of an apical view of the left ventricle of a 35-year-old male during the diastolic phase (i.e. as the ventricles fill with blood), acquired using the 4P1 transducer focused at 6 cm. Acquisition of the channel signals was triggered during diastole in order to minimize motion artifacts. On the left side of the B-mode image, the septal wall is partially visible, and on the right side, the lateral wall of the left ventricle is visible as the bright band extending from top to bottom of the image. The mitral valve is open and visible as the bright structure in the lower left of the image. Due to the rapid movement of the heart, individual channel signals for only a small FOV, consisting of 12 B-mode lines, from this image could be acquired in order to create the corresponding SLSC image in Fig. 7(b) and avoid significant corruption by cardiac motion.

The SLSC image demonstrates a considerable reduction in clutter in the ventricle, compared to the B-mode image. Harmonic B-mode imaging (Fig. 7(c)) shows better definition of the mitral valve (lower left of image), however definition of the endocardial border is not significantly better than the fundamental image, except for the lower portion of the border between 9 and 11 cm depth. In the HSCI image, a significant reduction in clutter is obtained within the heart chamber, and clear delineation of both the lateral and distal endocardial borders is obtained. The endocardial border definition is greater in the HSCI image than in the fundamental SLSC image. The contrast and CNR between the cardiac tissue located between 10 and 11 cm depth and the lumen of the ventricle is shown in Tab. II.

V. Discussion

While a B-mode image is a display of scatterer reflectivity where white is high reflectivity and black is little or no reflectivity, the SLSC image is a display of echo spatial coherence where white is high coherence and black is little or no coherence. Despite this fundamental difference, SLSC images are remarkably similar to B-mode images in appearance (although it is less susceptible to clutter because clutter is spatially incoherent, as shown in Fig. 5). It is important to keep in mind that the contrast and boundaries of the features in the SLSC and HSCI images are defined by changes in spatial coherence, rather than signal magnitude. Thus, two targets that may have similar echo magnitude but differing spatial coherence functions will have high contrast in the SLSC or HSCI image. Alternatively, objects that have vastly different magnitudes in the B-mode image may have similar coherence in the SLSC and HSCI images, and will therefore show no contrast. The texture in the SLSC and HSCI images is determined by the variance of the spatial coherence function in the short-lag region, as opposed to constructive and destructive wave interference in the B-mode image.

One important distinction must be made with regards to the creation of B-mode and SLSC (and HSCI) images. While B-mode images are often compressed using some form of logarithmic compression or grayscale mapping, the SLSC and HSCI images do not require compression or grayscale mapping, although moderate compression may be employed in particular cases of high noise [4]. Grayscale mapping is necessary in B-mode imaging because of the large dynamic range of echoes acquired from backscattered tissue. In SLSC and HSCI, the normalization process of equation 1 limits the dynamic range of the image. In addition, the pixel values of the SLSC and HSCI images are more uniform in their histograms whereas B-mode images are skewed toward the lower end of the dynamic range.

However, given these fundamental differences, the images shown here are made such that they display the best possible representation of the organ or target of interest. In addition the contrast, CNR, and speckle SNR measurements were performed prior to any compression or mapping such that they can be compared on the same scale.

The images depicted in Fig. 2 demonstrate fairly equal-quality images for the harmonic and fundamental versions of each imaging type. Subtle differences, either advantageous or disadvantageous, between imaging modes are visible, however each image yields accurate descriptions of the underlying tissue or tissue structure. These images, however, are derived from signals containing no noise. Fig. 3 demonstrates this same figure with the addition of acoustical noise and aberration. The advantages of SLSC and HSCI imaging become apparent in this figure, where acoustical noise is better suppressed than the conventional delay-and-sum beamformer.

For signals that are dominated by noise, such as the lumen region of a blood vessel where the echo backscattered by blood is small, as in Fig. 5, the spatial coherence function is approximately zero for all lags except lag 0 (which is identical to the autocorrelation of noise). Therefore, the area under the spatial coherence function is approximately zero. For tissue partially corrupted by noise, the spatial coherence function and the resulting V_{slsc} are functions of the signal-to-clutter ratio, but tend to zero as the strength of the noise increases. As shown in Fig. 5, echoes corrupted by acoustical noise show a sharp drop-off in coherence after lag 0, but then a gradual decrease for increasing lag. There are many sources of acoustical noise, however the primary sources responsible for these decreases in coherence are phase aberrations and reverberation clutter. The large lags of the spatial coherence function do not contribute much to the SLSC and HSCI images because the spatial coherence at these lags are not significantly different for noise, speckle signal, and corrupted signal.

The second harmonic signals in ultrasound are less susceptible to reverberation clutter because necessary propagation distance of the acoustical pulse in order to generate the second harmonic signal. Despite this advantage, harmonic signals are not immune to reverberation clutter, and they are sensitive (and perhaps more so than the fundamental) to phase aberrations, which increase sidelobes that result in clutter from off-axis scattering [22]. This is apparent in the simulated and *in vivo* images (Figs. 3, 4, 6, and 7) where the harmonic image show significant amounts of clutter.

Because the harmonic signals do not contain as strong reverberation clutter as the fundamental, the harmonic signals show greater coherence for the majority of lags, as demonstrated in Fig. 5. Thus, for the same amount of reverberation clutter, the HSCI image may show image features or contrast that may not be apparent in the SLSC image, such as the medulla/cortex interface in Fig. 6. In addition, the HSCI image will show a brighter and smoother background than the corresponding SLSC image formed from the fundamental signal. This is particularly apparent in the *in vivo* liver images (Fig. 4), where the background liver tissue appears brighter in the HSCI image than the SLSC image. The speckle SNR, a measure of the local variations or smoothness of the background tissue, shows larger values for HSCI compared to SLSC imaging (Tabs. II and I). For B-mode imaging, the theoretical value of speckle SNR is 1.9 regardless of the amount or type of clutter or imaging mode. For a wide range of image noise, SLSC and HSCI imaging will have greater speckle SNR than B-mode imaging. However, as the image noise or clutter increases to many times greater than the signal, the speckle SNR for SLSC and HSCI imaging will decrease to zero, while B-mode imaging will remain at 1.9 [4].

The contrast and CNR values displayed in Tabs. II and I indicate that SLSC imaging creates greater detectability of most targets and imaging structures due to decreased clutter and increased smoothness of background tissue. Some targets, such as high-intensity point targets, are likely to be poorly visualized in SLSC and HSCI images due to the normalization of echo magnitude. Although contrast does not always increase with SLSC or HSCI imaging, the CNR is a measure of the detectability of contrast changes with respect to the local image variance from speckle or clutter. In general, an object with a CNR around 0.9 is difficult to detect, although the actual cutoff for determining the presence of an object or target depends on the size of the target and the resolution of the imaging system [41]. Tab. II indicates that for the high-contrast *in vivo* targets presented in Figs. 4 and 7, SLSC imaging, and particularly HSCI, moves the targets from the undetectable range to the detectable range in terms of CNR. While the values for contrast, CNR, and speckle SNR change as a function of Q [3], these values are generally better if Q is kept within the short-lag region.

The values of Q (Eq. 2) in the simulations are often much larger than the Q used in the *in vivo* liver, kidney, and heart. In general, the amount of noise in the *in vivo* channel signals often cause the spatial coherence functions to decrease more rapidly than that of the simulations (and experiments in tissue-mimicking phantoms [3]). Increasing Q beyond the values used in these *in vivo* experiments tends to decrease image quality because the spatial coherence function is approximately zero beyond this range of Q. The difference in Q required to obtain optimal visualization of the simulated thrombi is due to a smaller roll-off of the spatial coherence function in this particular simulation. As a clinical imaging mode, Q may be made available to the clinician or sonographer by use of a knob control to adjust Q, although the values used here may be used as a starting point for the default image.

The majority of targets presented in these images are high-contrast targets. It has previously been shown, however, that SLSC imaging yields major improvements in contrast, CNR, and SNR for low-contrast targets as well [3, 4]. We hypothesize that HSCI will yield similar improvements consistent with these results for low-contrast targets, as suggested by the visualization of the low-contrast structures in Fig. 6.

VI. Conclusions

A harmonic version of SLSC imaging, called Harmonic Spatial Coherence Imaging (HSCI), was demonstrated on *in vivo* human livers and human hearts and on a simulated heart chamber using a full-wave, nonlinear-propagation, simulation tool. Fundamental SLSC and HSCI images are similar in appearance to B-mode images, however their underlying construction are substantially different than conventional ultrasound imaging. HSCI showed improved performance over harmonic B-mode imaging as well as better performance over fundamental SLSC imaging.

HSCI showed better reduction of clutter than harmonic B-mode and fundamental SLSC imaging, and improved the delineation of target borders and the detectability of objects. The CNR of *in vivo* targets improved by 0.2–0.3 in harmonic B-mode imaging, 0.8–0.9 in fundamental SLSC imaging, and 1.1–1.3 in HSCI imaging compared to fundamental B-mode imaging. Superior speckle SNR was obtained in HSCI because of greater spatial coherence and low reverberation clutter in the second harmonic of the echo backscatter. In human livers, speckle SNR was measured to be 1.9 for fundamental and harmonic B-mode imaging, whereas fundamental SLSC imaging increased speckle SNR to 2.7 and HSCI increase speckle SNR to 3.4.

Acknowledgments

This work is supported by NIH grants R21-EB008481 from the National Institute of Biomedical Imaging and Bioengineering and R01-CA114093 from the National Cancer Institute. The authors wish to thank the Ultrasound Division at Siemens Medical Solutions USA, Inc. for their in-kind and technical support.

References

1. Szabo, TL. Diagnostic Ultrasound Imaging: Inside Out. London, UK: Elsevier Academic Press;
2. Wagner RF, Smith SW, Sandrik JM, Lopez H. Statistics of speckle in ultrasound b-scans. IEEE Trans Sonics Ultrason. 1983; 30(3):156–163.
3. Lediju M, Trahey GE, Byram BC, Dahl JJ. Short-lag spatial coherence of backscattered echoes: Imaging characteristics. IEEE Trans Ultrason Ferroelect Freq Contr. 2011; vol. 58(no. 7):1377–1388.
4. Dahl JJ, Hyun D, Lediju M, Trahey GE. Lesion detectability in diagnostic ultrasound with short-lag spatial coherence imaging. Ultrason Imaging. 2011; vol. 33(no. 2):119–133. [PubMed: 21710827]
5. Uppot RN, Sahani DV, Hahn PF, Kalra MK, Saini SS, Mueller PR. Effect of obesity on image quality: fifteen-year longitudinal study for evaluation of dictated radiology reports. Radiology. 2006; vol. 240(no. 2):435–439. [PubMed: 16801372]
6. Shmulewitz A, Teefey SA, Robinson BS. Factors affecting image quality and diagnostic efficacy in abdominal sonography: A prospective study of 140 patients. J Clin Ultrasound. 1993; vol. 21(no. 9):623–630. [PubMed: 8227392]
7. Garrett JV, Passman MA, Guzman RJ, Dattilo JB, Naslund TC. Expanding options for bedside placement of inferior vena cava filters with intravascular ultrasound when transabdominal duplex ultrasound imaging is inadequate. Ann Vasc Surg. 2004; vol. 18(no. 3):329–334. [PubMed: 15354635]
8. Khoury FR, Ehrenberg HM, Mercer BM. The impact of maternal obesity on satisfactory detailed anatomic ultrasound image acquisition. J Matern Fetal Neonatal Med. 2009; vol. 22(no. 4):337–341. [PubMed: 19085631]
9. Averkiou MA, Roundhill DN, Powers JE. A new imaging technique based on the nonlinear properties of tissues. Proc IEEE Ultrason Symp. 1997; vol. 2:1561–1566.
10. Christopher T. Finite amplitude distortion-based inhomogeneous pulse echo ultrasonic imaging. IEEE Trans Ultrason Ferroelect Freq Contr. 1997; vol. 44(no. 1):125–139.
11. Ward B, Baker AC, Humphrey VF. Nonlinear propagation applied to the improvement of resolution in diagnostic medical ultrasound. J Acoust Soc Am. 1997; vol. 101(no. 1):143–154. [PubMed: 9000731]
12. Spencer KT, Bednarz J, Rafter PG, Korcarz C, Lang RM. Use of harmonic imaging without echocardiographic contrast to improve two-dimensional image quality. Am J Cardiol. 1998; vol. 82(no. 6):794–799. [PubMed: 9761093]
13. Tranquart F, Grenier N, Eder V, Pourcelot L. Clinical use of ultrasound tissue harmonic imaging. Ultrasound Med Biol. 1999; vol. 25(no. 6):889–894. [PubMed: 10461715]
14. Rosen EL, Soo MS. Tissue harmonic imaging sonography of breast lesions: Improved margin analysis, conspicuity image quality compared to conventional ultrasound. Clin Imaging. 2001; vol. 25(no. 6):379–384. [PubMed: 11733148]
15. Mallart R, Fink M. Adaptive focusing in scattering media through sound-speed inhomogeneities: The van Cittert Zernike approach and focusing criterion. J Acoust Soc Am. 1994; vol. 96(no. 6):3721–3732.
16. Hollman KW, Rigby KW, O’Donnell M. Coherence factor of speckle from a multi-row probe. Proc IEEE Ultrason Symp. 1999; vol. 2:1257–1260.
17. Liu D-L, Waag RC. Correction of ultrasonic wavefront distortion using backpropagation and a reference waveform method for time-shift compensation. J Acoust Soc Am. 1994; vol. 96(no. 2):649–660. [PubMed: 7930065]
18. Li P-C, Li M-L. Adaptive imaging using the generalized coherence factor. IEEE Trans Ultrason Ferroelect Freq Contr. 2003; vol. 50(no. 2):128–141.

19. Krishnan S, Li PC, O'Donnell M. Adaptive compensation of phase and magnitude aberrations. IEEE Trans Ultrason Ferroelect Freq Contr. 1996; vol. 43(no. 1):44–55.
20. Camacho J, Parrilla M, Fritsch C. Phase coherence imaging. IEEE Trans Ultrason Ferroelect Freq Contr. 2009; vol. 5(no. 5):958–974.
21. Dahl JJ, Pinton GF. Characterization of clutter in ultrasonic imaging using a nonlinear full-wave simulation method and in vivo human tissue. J Acoust Soc Am. 2010; vol. 127(no. 3 pt. 2):1866.
22. Pinton GF, Trahey GE, Dahl JJ. Erratum: Sources of image degradation in fundamental and harmonic ultrasound imaging: A nonlinear fullwave simulation study. IEEE Trans Ultrason Ferroelect Freq Contr. 2011; vol. 58(no. 6):1272–1283.
23. Lediju M, Pihl MJ, Hsu SJ, Dahl JJ, Gallippi CM, Trahey GE. A motion-based approach to abdominal clutter rejection. IEEE Trans Ultrason Ferroelect Freq Contr. 2009; vol. 56(no. 11): 2437–2449.
24. Mauldin, FW., Jr; Lin, D.; Hossack, JA. A singular value filter for rejection of stationary artifact in medical ultrasound; Proc IEEE Ultrason Symp; 2010. p. 359-362.
25. Flax SW, O'Donnell M. Phase-aberration correction using signals from point reflectors and diffuse scatterers: Basic principles. IEEE Trans Ultrason Ferroelect Freq Contr. 1988; vol. 35(no. 6):758–767.
26. Nock L, Trahey GE, Smith SW. Phase aberration correction in medical ultrasound using speckle brightness as a quality factor. J Acoust Soc Am. 1989; vol. 85(no. 5):1819–1833. [PubMed: 2732378]
27. Fink M. Time reversal of ultrasonic fields - part I: Basic principles. IEEE Trans Ultrason Ferroelect Freq Contr. 1992; vol. 39(no. 5):555–566.
28. Rigby KW, Andarawis EA, Chalek CL, Haider BH, O'Donnell M, Smith LS, Wildes DG. Improved *In Vivo* abdominal image quality using real-time estimation and correction of wavefront arrival time errors. Proc IEEE Ultrason Symp. 2000; vol. 2:1645–1653.
29. Dahl JJ, McAleavey SA, Pinton GF, Soo MS, Trahey GE. Adaptive imaging on a diagnostic ultrasound scanner at quasi real-time rates. IEEE Trans Ultrason Ferroelect Freq Contr. 2006; vol. 53(no. 10):1832–1843.
30. Dahl JJ, Feehan TJ. Direction of arrival filters for improved aberration estimation. Ultrason Imaging. 2008; vol. 30(no. 1):1–20. [PubMed: 18564593]
31. Goodman, JW. Statistical Optics. New York, New York: John Wiley & Sons, Inc.; 1985.
32. Mallart R, Fink M. The van Cittert-Zernike theorem in pulse echo measurements. J Acoust Soc Am. 1991; vol. 90(no. 5):2718–2727.
33. Walker WF, Trahey GE. Speckle coherence and implications for adaptive imaging. J Acoust Soc Am. 1997; vol. 101(no. 4):1847–1858. [PubMed: 9104014]
34. Fedewa RJ, Wallace KD, Holland MR, Jago JR, Ng GC, Rielly MR, Robinson BS, Miller JG. Spatial coherence of backscatter for the nonlinearly produced second harmonic for specific transmit apodizations. IEEE Trans Ultrason Ferroelect Freq Contr. 2004; vol. 51(no. 5):576–588.
35. Chapman, CS.; Lazenby, JC. Ultrasound imaging system employing phase inversion subtraction to enhance the image. U.S. Patent. 5,632,277.
36. Pinton GF, Dahl JJ, Rosenzweig S, Trahey GE. A heterogeneous nonlinear attenuating full-wave model of ultrasound. IEEE Trans Ultrason Ferroelect Freq Contr. 2009; vol. 56(no. 3):474–488.
37. Hinkelman LM, Metlay LA, Churukian CJ, Waag RC. Modified Gomori trichrome stain technique for macroscopic tissue slices. J Histotech. 1996; vol. 19(no. 4):321–323.
38. Mast TD, Hinkelman LM, Orr MJ, Sparrow VW, Waag RC. Simulation of ultrasonic pulse propagation through the abdominal wall. J Acoust Soc Am. 1997; vol. 102(no. 2):1177–1190. [Erratum: J Acoust Soc Am 104, 1124-1128 (1998)]. [PubMed: 9265762]
39. Brunke SS, Insana MF, Dahl JJ, Hansen C, Ashfaq M, Ermert H. An ultrasound research interface for a clinical system. IEEE Trans Ultrason Ferroelect Freq Contr. 2007; vol. 54(no. 1):198–210.
40. Dahl JJ, Soo MS, Trahey GE. Spatial and temporal aberrator stability for real-time adaptive imaging. IEEE Trans Ultrason Ferroelect Freq Contr. 2005; vol. 52(no. 9):1504–1517.
41. Smith SW, Wagner RF, Sandrik JM, Lopez H. Low contrast detectability and contrast/detail analysis in medical ultrasound. IEEE Trans Sonics Ultrason. 1983; vol. 30(no. 3):164–173.

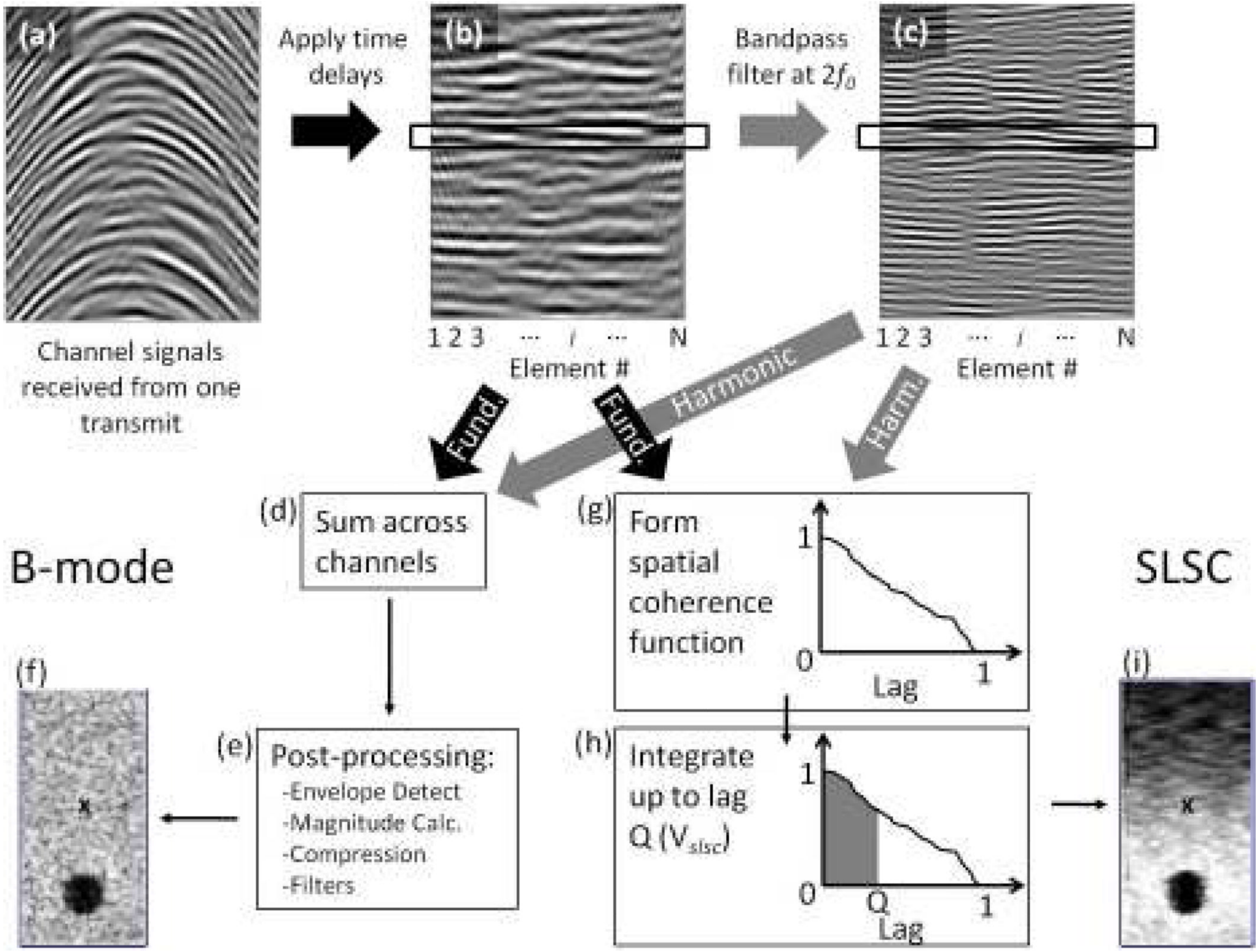

Fig. 1.

The processes of forming B-mode and SLSC images. (a) First, the echoes from a pulse are recorded by the transducer elements. (b) Time delays are applied to the echoes. The echoes can then be used to form B-mode or SLSC images, or they can be (c) bandpass filtered at the second harmonic frequency, $2f_0$ for harmonic B-mode or HSCI imaging. For B-mode images, the echoes in (b) or (c) are (d) summed across the elements and then (e) passed through several post processing steps to arrive at (f) the B-mode image. For SLSC (and HSCI) imaging, (g) the echoes within the black box in (b) or (c) are cross-correlated with one another to form a spatial coherence function. (h) The spatial coherence function is integrated up to lag Q to obtain the pixel value in (i) the SLSC image. Steps (g) and (h) are repeated over depth for each pulse-echo over a FOV to form an image. The pixel value labeled ’x’ in the SLSC image (i) has a corresponding pixel value in the B-mode image (e).

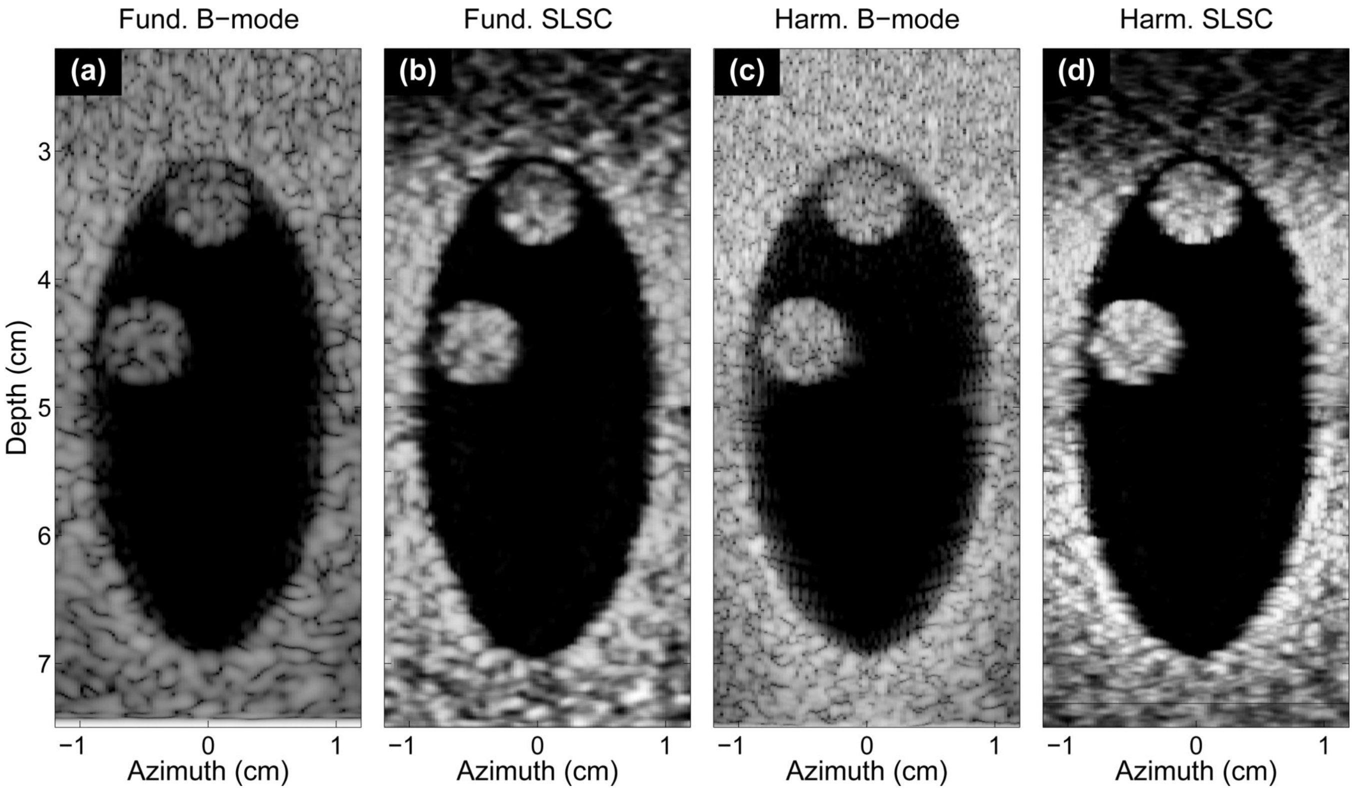

Fig. 2.

(a) B-mode, (b) SLSC, (c) harmonic B-mode, and (d) HSCI images of a simulated heart chamber with no intervening skin and subcutaneous layers and two thrombi located at 35 and 45mm depth. Both thrombi are visible in all images. The SLSC and HSCI images show smoother background and tissue layers, but also delineate the space between the thrombi and the chamber walls in better detail than the two B-mode images.

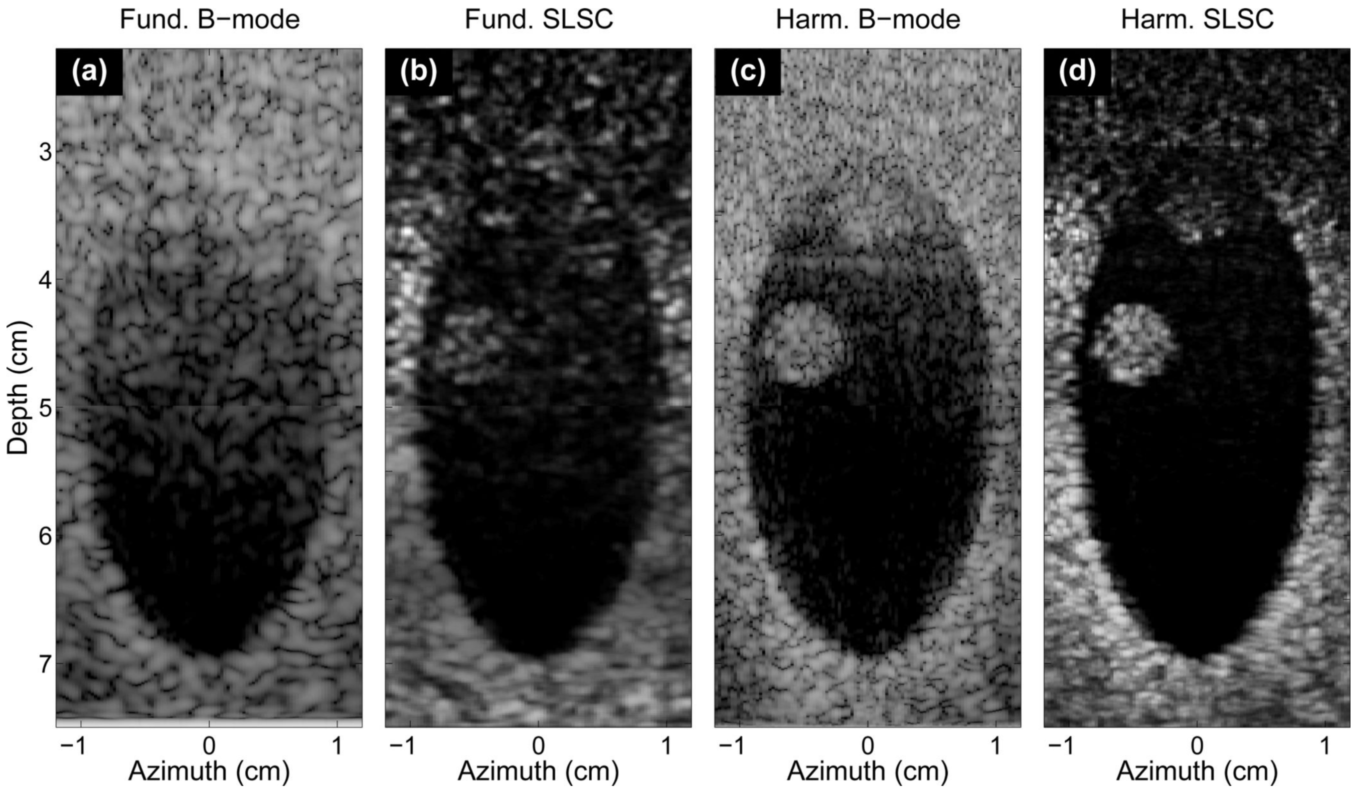

Fig. 3.

The same (a) B-mode, (b) SLSC, (c) harmonic B-mode, and (d) HSCI images as in Fig. 3 with intervening skin and subcutaneous tissue layers. Neither thrombi is visible within the clutter of the fundamental B-mode image. The thrombus at 45mm, however, is visible in SLSC image where clutter has been suppressed. The harmonic B-mode also reduces clutter and shows good visualization of the thrombus at 45mm, although clutter obscures the other thrombus. The HSCI image shows good delineation of the chamber walls and both thrombi while reducing clutter. Depth-dependent gain is applied to the SLSC images to minimize depth-dependent brightness variations.

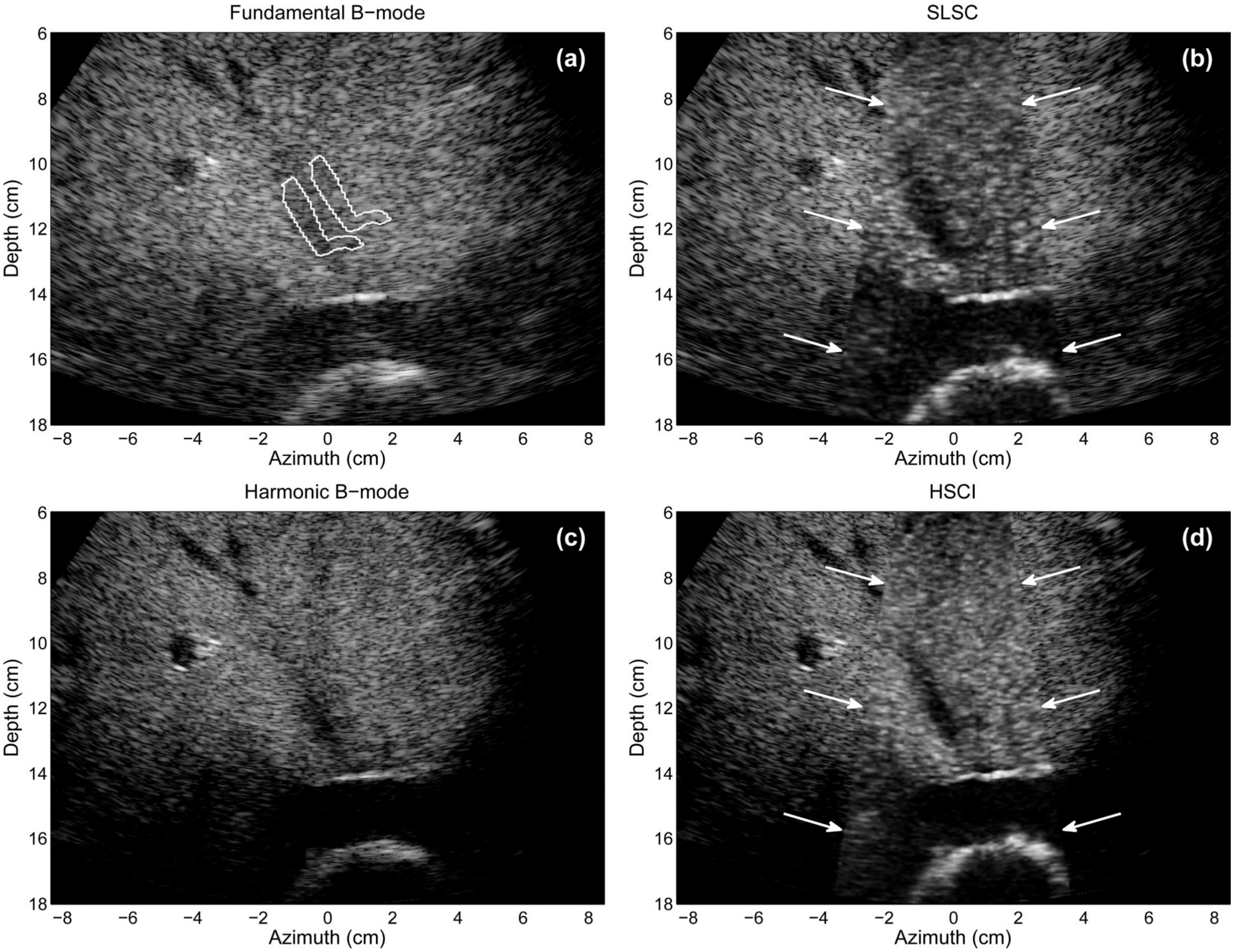

Fig. 4.

(a) Fundamental B-mode, (b) SLSC, (c) harmonic B-mode, and (d) HSCI images of the liver of a 57-year-old male. Arrows demarcate the boundaries of the SLSC and HSCI images. The vertically aligned vessel at 10–13 cm is better visualized in the SLSC and HSCI images. Delineation of a branch off of this vessel is observed in the SLSC and HSCI images which is not visible in the B-mode image. Brighter background is observed in the HSCI image compared to the SLSC image due to the improved coherence of the harmonic signal. The B-mode images show 35 dB of dynamic range while the SLSC images show approximately full linear scale. The countour lines in (a) indicate the regions used for quantitative measures.

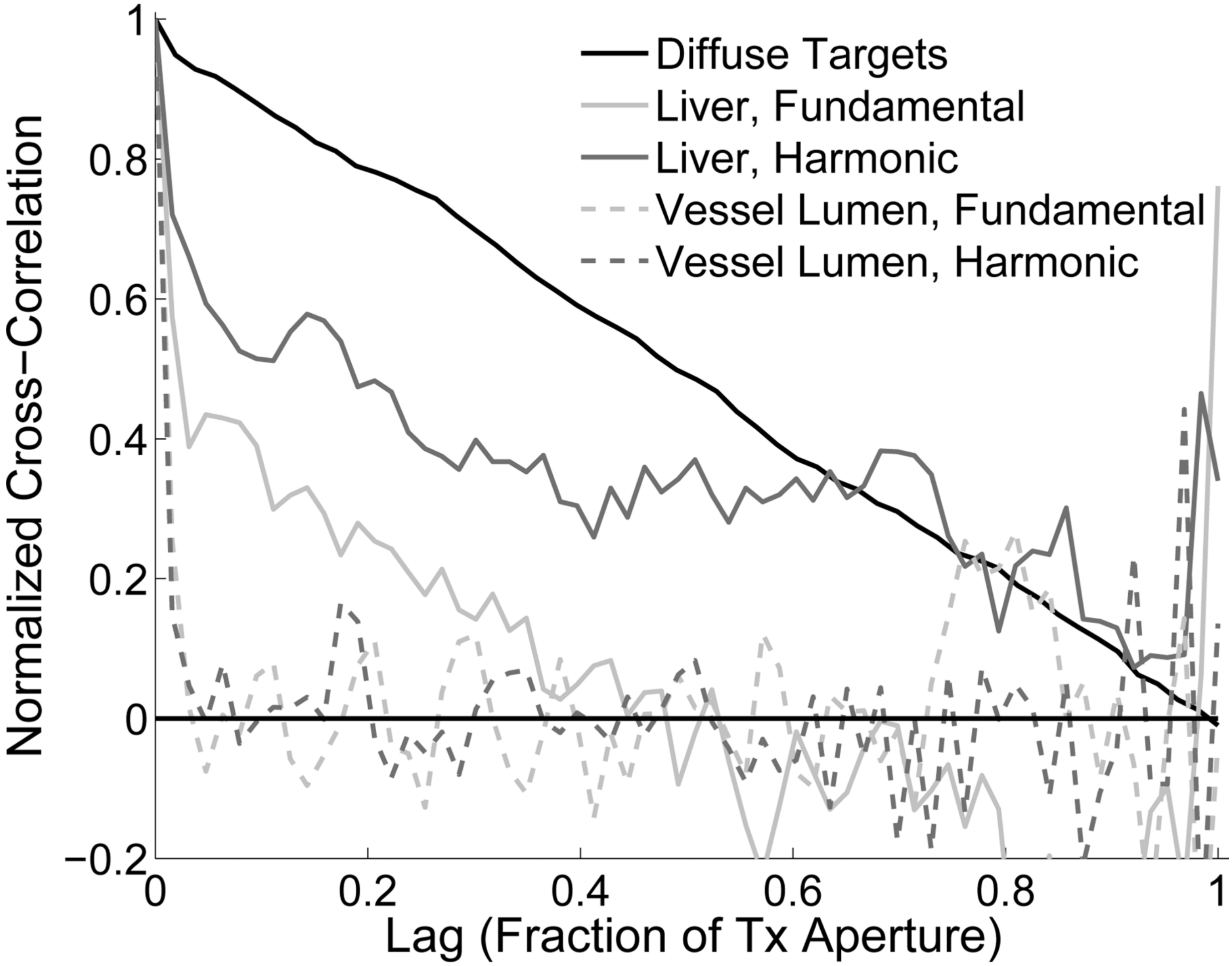

Fig. 5.

The spatial coherence functions of echoes from diffuse scatterers, liver tissue (fundamental and harmonic), and liver vasculature. SLSC imaging differentiates these echoes because of their differences in spatial coherence, whereas B-mode imaging differentiates the echoes based on their magnitude.

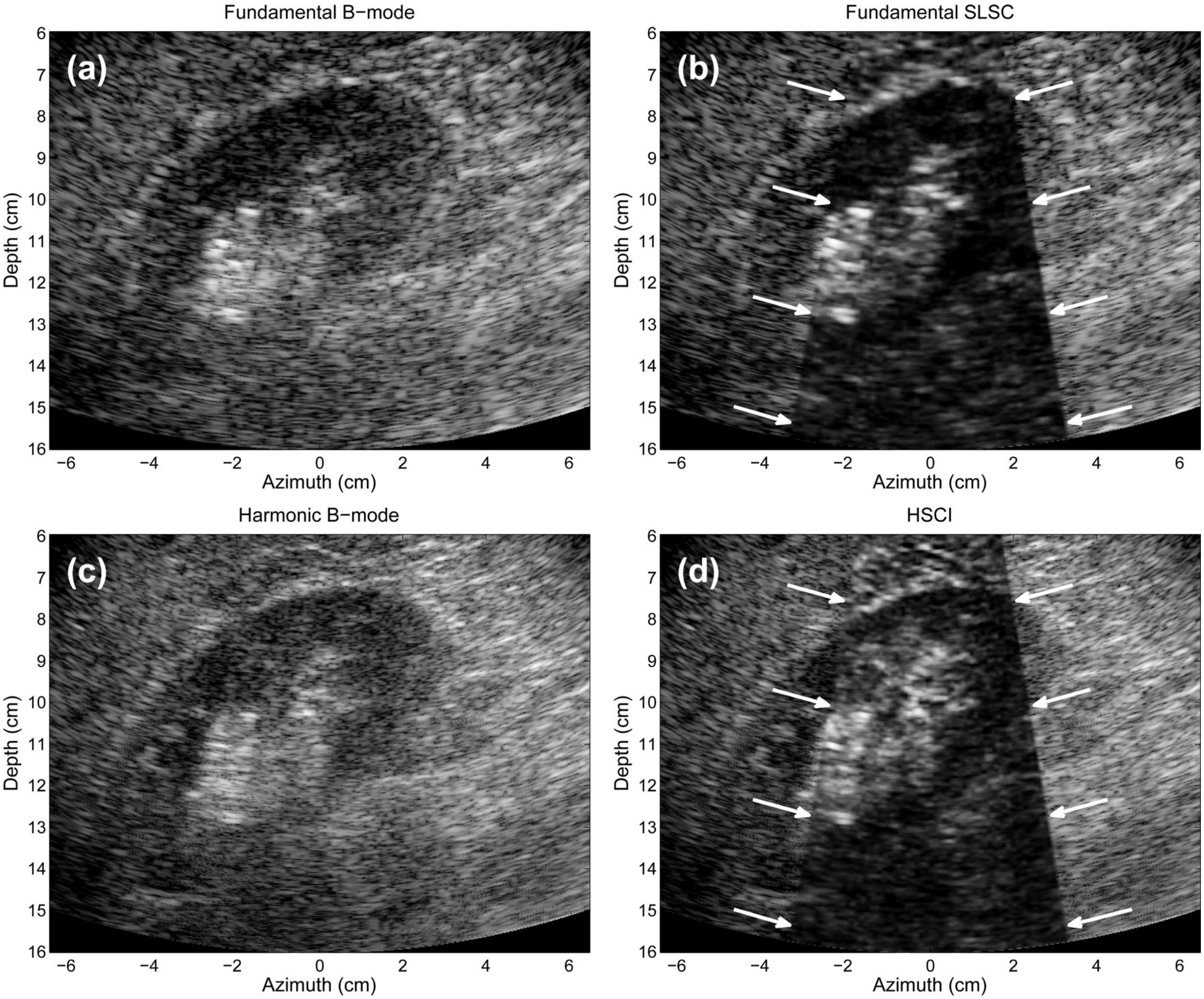

Fig. 6.

(a) Fundamental B-mode, (b) SLSC, (c) harmonic B-mode, and (d) HSCI images of the right kidney in a 57-year-old male. The transmit pulses are focused at 10 cm depth. The SLSC and HSCI images show greater detail that is not apparent in the fundamental and harmonic B-mode images. The SLSC and HSCI images also show superior clutter reduction than the harmonic B-mode image. The B-mode images show 45 dB of dynamic range while the SLSC images show approximately full linear scale.

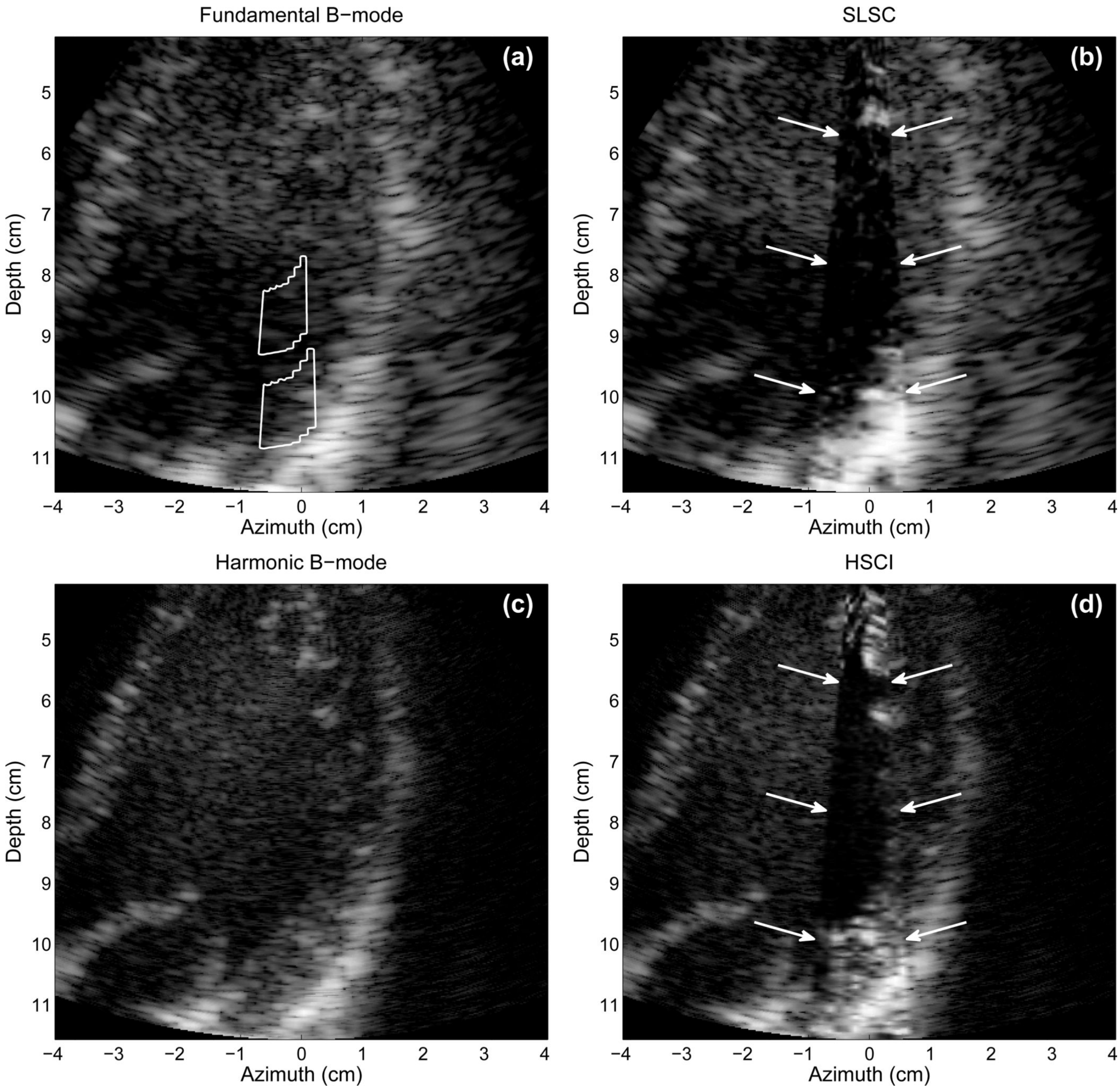

Fig. 7.

Fundamental (a) B-mode and (b) SLSC images of an apical view of the left ventricle. Harmonic (c) B-mode and (d) HSCI images of the same view of the heart. The SLSC and HSCI images are shown as a small sector inserted into the B-mode image. The SLSC and HSCI images show little clutter within the ventricular chamber compared to the B-mode images. The endocardial border on the lateral wall of the ventricle is visible in the HSCI image but not visible in any of the other images. The countour lines in (a) demarcate the regions used for quantitative measures.

Table 1

Thrombus contrast, CNR, and SNR.

Figure	Contrast (dB)	CNR	SNR
2(a) Fund. B-mode	34	1.6	1.7
2(b) SLSC	25	3.0	2.9
2(c) Harm. B-mode	40	1.3	1.3
2(d) HSCI	22	3.8	3.6
3(a) Fund. B-mode	3	0.5	2.1
3(b) SLSC	8	1.4	2.6
3(c) Harm. B-mode	18	1.5	1.7
3(d) HSCI	21	3.5	3.9

Table 2

Contrast, CNR, and SNR from in vivo images

Figure	Mode	Contrast (dB)	CNR	SNR
4(a)	Fund. B-mode	3	0.4	1.9
4(b)	SLSC	7	1.2	2.7
4(c)	Harm. B-mode	5	0.6	1.9
4(d)	HSCI	8	1.5	3.4
7(a)	Fund. B-mode	11	0.6	N/A
7(b)	SLSC	13	1.5	N/A
7(c)	Harm. B-mode	13	0.9	N/A
7(d)	HSCI	37	1.9	N/A